International Journal of Heat and Mass Transfer 146 (2020) 118837

Contents lists available at ScienceDirect

International Journal of Heat and Mass Transfer

journal homepage: www.elsevier.com/locate/ijhmt

Macroscopic transport properties of Gyroid structures based on pore-scale studies: Permeability, diffusivity and thermal conductivity

Ji-Wang Luo [a], Li Chen [a,*], Ting Min [b], Feng Shan [c], Qinjun Kang [d], WenQuan Tao [a]

[a] Key Laboratory of Thermo-Fluid Science and Engineering of MOE, School of Energy and Power Engineering, Xi'an Jiaotong University, Xi'an, Shaanxi 710049, China
[b] School of Chemical Engineering and Technology, Xi'an Jiaotong University, Xi'an, Shaanxi 710049, China
[c] AAC Technologies Holdings Inc., Nanjing University Science Park, Qixia District, Nanjing City, 224400 Jiangsu Province, China
[d] Computational Earth Science, EES-16, Earth and Environmental Sciences Division, Los Alamos National Laboratory, Los Alamos, NM 87544, USA

ARTICLE INFO

Article history:
Received 21 April 2019
Received in revised form 3 October 2019
Accepted 4 October 2019
Available online 15 October 2019

Keywords:
Gyroid structure
Pore-scale study
Permeability
Effective diffusivity and thermal conductivity
Tortuosity

ABSTRACT

Gyroid structure is a kind of triply periodic minimum surface, which presents several advantages such as free-standing, highly ordered and interconnected pore network and high specific surface area. Understanding transport processes inside the Gyroid structure is important for its application. In this study, porous structures of the Gyroid are reconstructed, and then pore-scale studies of fluid flow, diffusion and heat transfer in the two phases of Gyroid structures are numerically implemented using the lattice Boltzmann method (LBM). Pore-scale velocity, concentration and temperature fields inside the Gyroid structures are discussed, based on which macroscopic properties including permeability, effective diffusivity, effective thermal conductivity, and tortuosity are predicted. There are two phases in the Gyroid structures, and both phases are continuous, leading to the bicontinuous characteristic of Gyroid structures. The results show that transport resistance in one phase is lower than that in the other phase. Thus from the perspective of enhancing transport process, it is desirable to choose the phase with higher transport properties for transporting the slower process. The present study provides guidance for subsequent applications of Gyroid structure.

1. Introduction

Transport phenomenon in porous media is a very attracting engineering subject due to its wide practical applications [1]. Typical examples include porous electrodes of fuel cells and batteries, porous filters, porous heat exchangers and tissue engineering [2–4]. Designing and fabricating porous media with optimized architecture (porosity, specific surface area and pore size.), high transport properties (permeability, effective diffusivity and effective thermal conductivity.) and strong mechanics (elastic modulus and yield strength.) have long been pursued in a wide range of fields such as energy, environment, aerospace and aeronautical engineering and biomedical engineering [5]. Ordered porous media have many advantages such as high specific surface area, tunable pore sizes and shapes as well as good connection of different phases [6]. Different kinds of morphology of ordered porous media have been studied in the literature [6,7], such as simple face-centered and body-centered porous structures, fiber-based porous structures [8], open-cell porous foams [9] and lattice-based structures [10].

Among the ordered porous media, recently several kinds of intriguing porous media with periodic minimal surfaces have attracted growing attention. By definition, minimal surfaces have a mean curvature of zero at each point on the surface, and triply periodic minimal surfaces are a class of minimal surfaces that extend periodically in three directions. Gyroid is an important kind of triply periodic minimal surface. It was initially discovered by NASA scientist Alan Schoen in 1970 [11], and has been found in many self-assembling systems such as block copolymers, lipids and microemulsions, as well in nature such as soap film, cell membranes, and butterfly wings [12,13]. The Gyroid structure presents several advantages such as free-standing, highly ordered and interconnected pore network, and high specific surface area [14]. Such structure has the potential to provide both good transport and mechanical properties. Very recently, there have been some researches adopting Gyroid structures to enhance transport processes in energy conversion and storage devices. Crossland et al. [15] applied the Gyroid structure in a hybrid bulk heterojunction solar cell. It was found that the Gyroid structure performs well as organic hole transporting material, resulting in up to 1.7% power

* Corresponding author.
E-mail address: lichennht08@mail.xjtu.edu.cn (L. Chen).

https://doi.org/10.1016/j.ijheatmasstransfer.2019.118837
0017-9310/

conversion efficiency. Ichikawa, Kato and Ohno [16] constructed a proton conductive material based on the Gyroid structure. ChoudHury et al. [17] employed Gyroid structure in the cathode of lithium sulfur batteries, and found that the battery demonstrated high charging/discharging capacity, very good rate capacity, and high cycling stability over more than 200 cycles. Gao et al. [18] fabricated Polyoxometalate-based open framework with Gyroid structure, and obtained high proton conductivity. Kibsgaard, Jackson and Jaramillo [14] employed Gyroid structure as the morphology of a Pt_xNi alloy catalyst for oxygen reduction reaction in proton exchange membrane fuels. The catalyst remains intact and maintains high activity even after intensive accelerated stability testing. Werner et al. [19] adopted the two connecting phases in Gyroid structures as anode and cathode of Li-ion/sulfur battery, in which the cathode network and anode network are separated by the electrolyte coating. Stable open circuit voltage, reversible charge and discharge capacity were obtained.

In practice, porous media have been adopted for different purposes. In the mechanical field, usually elastic modulus and yield strength are the most important parameters [20]. For application in fields containing fluid flow and mass transport, which is concerned in the present study, transport properties, such as permeability, effective diffusivity, effective conductivity, are the research emphasis. For example, in electrical energy storage devices such as batteries, the achievable power depends on how fast this energy is accessible, which is usually limited by the diffusion and reaction of reactants in the porous electrodes [21]. Thus enhancing the transport is of great importance. There have been a few studies in the literature exploring transport capacity of Gyroid structures. Using finite volume method, Olivares et al. [22] numerically studied fluid flow in Gyroid and hexagonal scaffolds with porosity of 0.55 and 0.7. Distributions of velocity and shear stress were analyzed in detail. It was found that Gyroid architectures can provide a better fluid accessibility than the hexagonal structures. Ali and Sen [20] studied the potential utilization of scaffold with Gyroid structure in tissue engineering. Permeability and shear stress are important parameters for cell bioactivity. They adopted finite volume method to simulate fluid flow and predict permeability and wall shear stress in Gyroid structures and rectangular-pore lattice-based porous structures with different porosity. It was found that velocity field in the Gyroid structure is not uniform due to the complex morphology. Permeability was also predicted based on the velocity field numerically obtained. Ma et al. [23] fabricated Gyroid structures using 316L stainless steel via selective laser melting. Fluid flow was simulated in the Gyroid structures and the results show that Gyroid structures have close values of permeability compared with human cancellous bones. Recently, Shen et al. [24] numerically studied diffusion in lamellae, cylinders and Gyroid structures using random walks and coarse-grained Molecular simulations. Effective diffusivity in the two connecting phases of Gyroid structures was predicted.

Fluid flow and transport in porous media are usually observed physically and treated theoretically at two different scales: representative elementary volume (REV) scale and pore scale [25]. A REV of a porous medium is the smallest volume in which large fluctuations of observed quantities (such as porosity and permeability) no longer occur and thus scale characteristics of a porous flow hold. For studying transport phenomena in porous media at the REV scale, such as using Darcy equation or extended Darcy equations (Brinkman-Darcy and Forchheimer-Darcy equations) [26] for fluid flow in porous media, macroscopic transport properties are prerequisite to close the equation, for example permeability in Darcy equation. Progress in numerical methods and the increasing computational power have paved the way for pore-scale studies [27–30]. The pore-scale study directly resolves the realistic structures of a porous medium, and solves the first-principle equations, for example Navier-Stokes equation for fluid flow. Because the realistic structures are considered, structure statistic parameters and macroscopic transport properties are not prerequisite, but actually are post-processed from the porous structures and the detailed distributions of important variables (velocity, pressure, concentration and temperature) obtained from the pore-scale simulations. Traditional computational fluid dynamics (CFD) methods such as finite volume, finite element and finite difference methods encounter difficulties when generating grids for the complex porous structures and treating the complicated interfaces inside porous media. Mesoscopic numerical methods such as the lattice Boltzmann method (LBM), have the inherent capacity of accounting for the porous structures due to their remarkable ability of treating complex boundaries. The LBM has been widely adopted for simulating transport phenomena in porous media [21,31–33].

Based on the above literature review, it can be found that Gyroid structures have drawn increasing attention in the fields of energy storage, energy conversion and tissue engineering. However, thorough investigations of fluid flow and diffusion inside the Gyroid structures are still lack in the literature. In the present study, porous structures with Gyroid morphology are reconstructed. Fluid flow, diffusion and heat transfer inside the Gyroid structures are investigated in detail using the LBM. Based on the velocity, pressure, concentration and temperature fields obtained from the pore-scale simulations, permeability, effective diffusivity, thermal conductivity and tortuosity of the Gyroid structures are predicted. To the best of our knowledge, this is the first time the macroscopic transport properties of Gyroid structure are comprehensively studied.

2. Reconstruction of Gyroid structures

Since structure of the Gyroid is periodic, a unit cell of Gyroid structure is reconstructed based on the following equation [34]

$$\sin(a(i-1))\cdot\cos(a(j-1))+\sin(a(j-1))\cdot\cos(a(k-1)) + \sin(a(k-1))\cdot\cos(a(i-1))<b \quad (1)$$

where i, j and k represent coordinate components along x, y and z directions in Cartesian coordinates. a is a scaling factor calculated by

$$a=2\pi/l_L \quad (2)$$

where l_L is the size of the cubic unit cell. b is a parameter employed to control the volume fraction of different phases. Once a and b are determined, any point with coordinate (i, j, k) that satisfies Eq. (1) will be assigned as a node of phase B and that does not satisfy is set as a node of phase A, thus the unit cell of Gyroid structure with a certain size as well as a certain volume fraction of phase B f_B can be obtained. Higher value of b leads to higher f_B and lower f_A, and the summation of f_A and f_B equals unity. It is worth mentioning that the value of l_L should not be too small, since a fairly high resolution should be maintained in order to guarantee the connectivity of each phase. Besides, b ranges from 1.32 to 0.15 with the corresponding f_A ranges from 0.1 to 0.9. As mentioned previously, Gyroid structure is bicontinuous, indicating that both phase A and phase B can be served as the solid matrix. When phase B is the solid phase, the porosity is the same as the volume fraction of phase A, and vice versa.

The reconstruction process translates the Eq. (1) into concrete structures shown in Fig. 1. Fig. 1 shows the Gyroid structures reconstructed with porosity of ε_A (or f_A), where phase B is the solid matrix. The white part represents phase A and the blue region is phase B. Note that the Gyroid structure possesses the same archi-

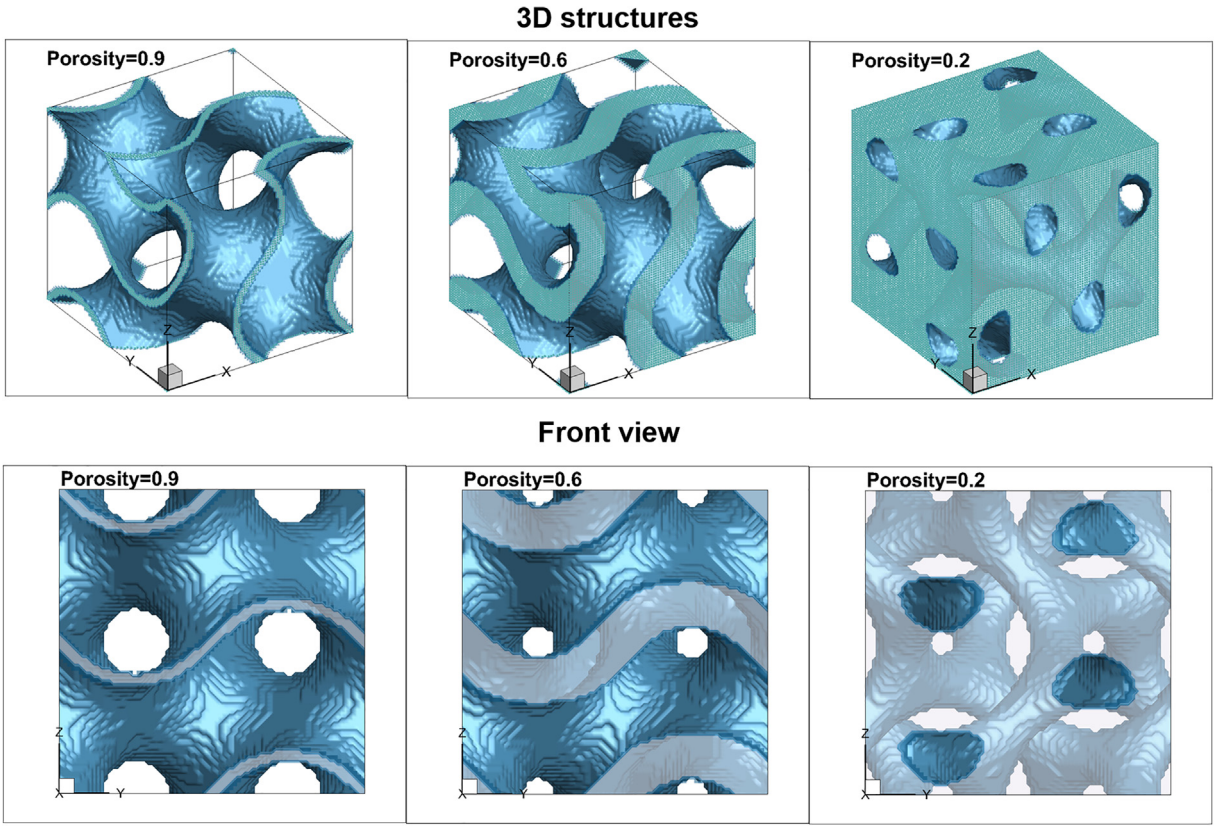

Fig. 1. Reconstructed porous structures of the Gyroid. Top row: 3D structures. Bottom row: front view. The white part is phase A, while the blue part is phase B. (For interpretation of the references to colour in this figure legend, the reader is referred to the web version of this article.)

tecture in all the three axes. From Fig. 1, it can be found that the Gyroid structure consists of two parts: three-dimensional interconnected phase A shown as white part and three-dimensional continuous phase B surrounding phase A shown as blue part. Both the two phases present good connectivity even under extremely low or high porosity. Such bicontinuous feature is highly desirable in a wide variety of applications. For example, in electrodes of proton exchange membrane fuel cells, multiple reactants are required to be transported including gas species, proton and electron. The Gyroid structure consists of bicontinuous phases which can transport gas and charge carriers simultaneously [35]. In a very recent study, Werner et al. [19] adopted the two connecting phases as anode and cathode of Li-ion/sulfur battery, in which the cathode network and anode network are separated by electrolyte coating. Such design greatly reduces the transport length and increases the contact area between the anode and cathode sides.

3. Numerical method

The LBM is adopted to simulate fluid flow, mass transport and heat transfer in the Gyroid structure reconstructed. The LB models adopted are briefly introduced as follows. For fluid flow, the multiple relaxation time (MRT) LB flow model is adopted, and the evolution equation for the distribution functions is follows

$$f_i(\mathbf{x}+\mathbf{e}_i\Delta t, t+\Delta t) - f_i(\mathbf{x},t) = \mathbf{Q}^{-1}\hat{\mathbf{S}}\mathbf{Q}[f_i^{eq}(\mathbf{x},t) - f_i(\mathbf{x},t)] \quad i = 0 \sim N \tag{3}$$

where $f_i(\mathbf{x},t)$ is the ith density distribution function at the lattice site $\mathbf{x}$ and time t. For the D3Q19 (three-dimensional nineteen-velocity) lattice model with $N = 18$, the discrete lattice velocity $\mathbf{e}_i$ is given by 0, $i = 0$; $((\pm1,0,0),\ (0,\pm1,0),\ (0,\pm1,0))$, $i = 1\sim6$; and$(\pm1,\pm1,0),\ (0,\pm1,\pm1),\ (\pm1,0,\pm1)$, $i = 7\sim18$. The equilibrium distribution function f_i^{eq} is as follows

$$f_i^{\mathbf{eq}} = w_i\rho\left[1 + \frac{\mathbf{e}_i\cdot\mathbf{u}}{(c_s)^2} + \frac{(\mathbf{e}_i\cdot\mathbf{u})^2}{2(c_s)^4} - \frac{\mathbf{u}\cdot\mathbf{u}}{2(c_s)^2}\right] \tag{4}$$

with the weight coefficient w_i as $w_i = 1/3$, $i = 0$; $w_i = 1/18$, $i = 1,2,\ldots,6$; $w_i = 1/36$, $i = 7,8,\ldots,18$. $c_s = 1/\sqrt{3}$ is the speed of sound.

$\mathbf{Q}$ in Eq. (3) is the transformation matrix, which transfers the distribution functions in velocity space into moment space [36]. $\mathbf{Q}^{-1}$ is the inverse matrix of $\mathbf{Q}$. $\hat{\mathbf{S}}$ is the relaxation matrix. The transformation matrix $\mathbf{Q}$ is constructed based on the principle that the relaxation matrix $\hat{\mathbf{S}}$ in moment space can be reduced to a diagonal matrix [36,37] with the diagonal terms as follows

$$s_0 = s_3 = s_5 = s_7 = 0,\ s_1 = s_2 = s_{9-15} = \frac{1}{\tau},$$
$$s_4 = s_6 = s_8 = s_{16-18} = 8\frac{2\tau-1}{8\tau-1} \tag{5}$$

The relaxation time τ is related to the fluid viscosity. Density and momentum are determined by sum of the distribution functions

$$\tau = \frac{\upsilon}{c_s^2\Delta t} + 0.5,\ \rho = \sum_i f_i,\ \mathbf{j} = \sum_i f_i\mathbf{e}_i \tag{6}$$

More details of the model can be found in Ref. [8].

For pure diffusion or heat conduction processes, the evolution of the distribution functions is as follows [38–40]

$$g_i(\mathbf{x}+\mathbf{e}_i\Delta t, t+\Delta t) - g_i(\mathbf{x},t) = \mathbf{R}^{-1}\bar{\mathbf{S}}\mathbf{R}(g_i^{eq} - g_i) \tag{7}$$

where g_i is the distribution function for a scalar, such as temperature or concentration. g_i^{eq} is the equilibrium distribution function:

$$g_i^{eq} = \begin{cases} (1-18k)\phi, & i = 0 \\ k\phi, & i = 1,2,\ldots,18 \end{cases} \tag{8}$$

where $k \in (0,1/18)$, in this study k is 1/20. ϕ represents temperature T or concentration C. $\mathbf{R}$ is a transformation matrix that transforms the velocity space into the moment space, and $\bar{\mathbf{S}}$ is relaxation matrix

$$\bar{\mathbf{S}}^{-1} = \begin{bmatrix} \tau_0 & & & & & & & & & & & & & & & & & & \\ & \tau_1 & & & & & & & & & & & & & & & & & \\ & & \tau_2 & & & & & & & & & & & & & & & & \\ & & & \tau_{xx} & 0 & \tau_{xy} & 0 & \tau_{xz} & & & & & & & & & & & \\ & & & 0 & \tau_4 & 0 & 0 & 0 & & & & & & & & & & & \\ & & & \tau_{yx} & 0 & \tau_{yy} & 0 & \tau_{yz} & & & & & & & & & & & \\ & & & 0 & 0 & 0 & \tau_6 & 0 & & & & & & & & & & & \\ & & & \tau_{zx} & 0 & \tau_{yz} & 0 & \tau_{zz} & & & & & & & & & & & \\ & & & & & & & & \tau_8 & & & & & & & & & & \\ & & & & & & & & & \ddots & & & & & & & & & \\ & & & & & & & & & & \tau_{18} & & & & & & & & \end{bmatrix} \tag{9}$$

For isotropic diffusion or heat conduction problems, $\tau_{xx} = \tau_{yy} = \tau_{zz}$, and $\tau_{ij} = 0$ $(i \neq j)$. The relaxation time can be expressed as:

$$(\tau_{ij})_k = \frac{1}{2}\delta_{ij} + \frac{(D_{ij})_k}{\varepsilon c^2 \Delta t}, \; i, j = 1,3 \tag{10}$$

where δ_{ij} is Kronecker symbol; c is the pseudo sound speed. The value of c should ensure the value of τ_{ii} $(i = 1,2,3)$ from 0.5 to 2. τ_0, τ_4, τ_5, τ_6 are generally set as unity without affecting the simulation results. More details of the LB model for heat and mass transfer can be found in Ref. [41].

Note that the in-house LB code developed in our group is written in Fortran and parallelized by message passing interface (MPI) technique.

4. Results and discussion

In this section, fluid flow, mass transport, and heat transfer inside the Gyroid structure are simulated at the pore scale. Important macroscopic transport properties including permeability, effective diffusivity, effective thermal conductivity and tortuosity are predicated.

4.1. Single-phase flow and permeability

In this section, single-phase fluid flow inside phase A (or phase B) of the Gyroid structure is simulated using the MRT LB fluid flow model introduced in Section 3. For studying fluid flow in phase A, phase B is considered as impermeable solid phase, and vice versa. The fluid density ρ and the relaxation time τ are set to be unity, thus the viscosity in LB unit can be obtained according to Eq. (6). A pressure gradient is applied along the x direction, which is implemented in the LB framework by using the extrapolation scheme [42]. The pressure gradient should be sufficiently low, in the present study 2×10^{-5}, to guarantee the validation of Darcy's law (Eq. (13)). Periodic boundary condition is adopted in the y and z direction. For the fluid-solid interface, no-slip boundary condition is applied, which is achieved in the LB framework by adopting the modified bounce-back scheme.

Before presenting the pore-scale results, grid independency check is conducted. Along each direction, five grid numbers from 40 to 200 grids with interval of 40 are adopted to discretize the Gyroid structure reconstructed in Section 2. Here, the structure with porosity of 0.1 is selected, which requires more grids to resolve the void space compared with other cases. The grid independency check is conducted for all the three processes studied including fluid flow, heat transfer and mass transport. The relative error of the parameter ϕ concerned is calculated by

$$\text{Relative error} = \frac{\left|\phi - \widehat{\phi}\right|}{\phi} \tag{11}$$

$\widehat{\phi}$ represents the value obtained from the finest resolution (highest grid number). Fig. 2 shows the relative error of permeability, effective diffusivity and effective thermal conductivity. If relative error lower than 2% is acceptable, it can be found that for fluid flow and diffusion processes which are only allowed inside the void space, the grid number of 160 grids along each direction is required, while for the heat transfer process which can take place in both solid and void space, 80 grids along each direction are sufficient.

Now attention is turned to the fluid flow in the Gyroid structure. Fig. 3 shows the velocity field obtained by the LB simulations, in which u is calculated as $\sqrt{u_x^2 + u_y^2 + u_z^2}$ and u_{max} is the maximum u. It can be found that the complex porous structures of Gyroid lead to complicated flow fields with high heterogeneity. It is worth mentioning that Gyroid structure is bicontinuous, which means that both phase A and B can be the solid matrix. Therefore, when simulating fluid flow in phase A, phase B is the solid matrix, and vice versa.

Based on the known velocity field, the Reynolds number, a significant dimensionless parameter indicating the characteristic of fluid flow, can be calculated by

$$Re = \frac{\overline{u_x} l_L}{\upsilon} \tag{12}$$

where $\overline{u}_x$ is superficial velocity, which is the averaged velocity along x direction in the entire domain including the solid phase. Since the pressure gradient ∇p is fixed during the simulations, the resulted Re varies with porosity as well as different transport phases. Table 1 lists all the Re for different cases studied.

Permeability k is one of the most important properties of porous media, which represents the ability of the porous media to transmit fluids. It can be calculated from the Darcy's law in the limit of low Reynolds number [43]

$$k = \frac{\overline{u}_x \mu}{\nabla p} \tag{13}$$

where μ is the dynamic viscosity. It is worth mentioning that Darcy's law is only valid for low Reynolds number flow, in which the role of inertia force can be neglected [44]. Under such circum-

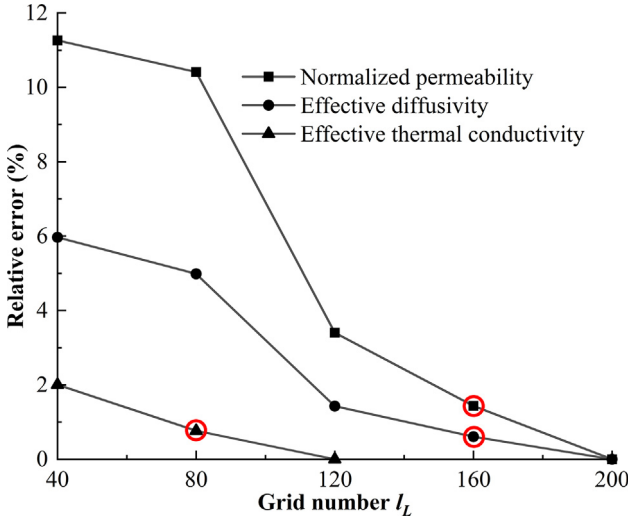

Fig. 2. Grid independency check. The relative error of permeability, effective diffusivity and effective thermal conductivity under different grid numbers.

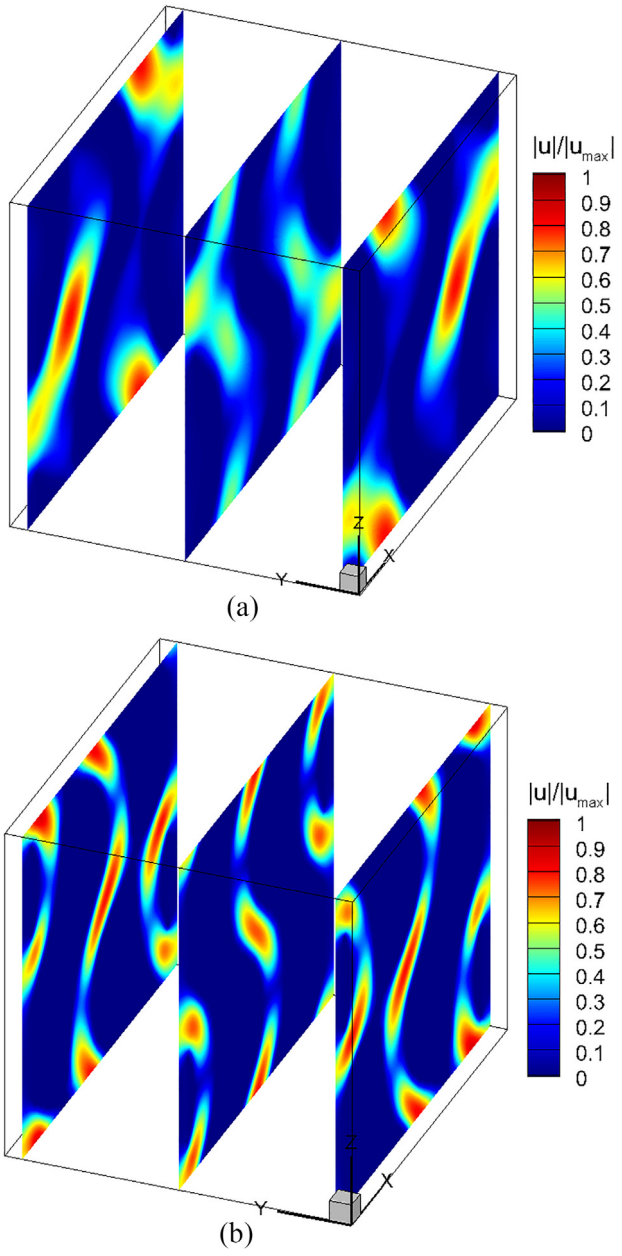

Fig. 3. Velocity filed in (a) phase A and (b) phase B of the Gyroid structure.

stance, permeability is only dependent on the porous structures, which is not affected by fluid properties and operating conditions, and the corresponding permeability is called intrinsic permeability. However, when Knudsen number, which is the ratio between the mean free path of gas and the characteristic pore size of a porous medium, is relatively high, the gas molecules tend to slip on the solid surface. Such slippage will increase the permeability, leading to the apparent permeability which is affected by fluid properties and operating conditions [44,45]. Study of the apparent permeability is out of scope of the present study.

Fig. 4 shows relationship between normalized permeability k/l_L^2 and porosity for different phases. As shown in Fig. 4, the value of permeability for phase A is higher than zero for the wide range of ε_A (0.1–0.9) studied, which is the same for phase B. This indicates good connectivity of both phase A and phase B in the Gyroid structure. That is why Gyroid structure is a bicontinuous material because each phase of the Gyroid is well connected. There have been a few studies in the literature for predicting permeability of phase A [20]. Results of Ali and Sen are also plotted in Fig. 4 for comparison. It can be found that agreement between our results and their results is acceptable. A wider range of ε_A is covered in the present study.

To the best of our knowledge, in the literature there has been no study regarding fluid flow in phase B. Using the LB model, fluid flow in phase B is further studied and the permeability is shown in Fig. 4. It can be found that permeability of phase B is higher than phase A after about porosity of 0.5; before that, it is slightly lower than phase A. This means that for the two phases in Gyroid structure, basically phase B has a higher capacity for fluid flow through. Besides, the increase of permeability of phase B is more profound under relatively higher ε_B.

4.2. Pure diffusion and effective diffusivity

In this section, pure diffusion process obeying the Fick's Law is simulated inside the Gyroid structure [46]

$$\nabla(\Gamma\nabla\xi) = 0 \tag{14}$$

Eq. (14) is applicable to, for example, heat conduction with Γ as thermal conductivity and ξ as temperature, gas diffusion with Γ as diffusivity and ξ as concentration, or electron (proton) conduction with Γ as conductivity and ξ as potential. Without loss of generality, here the diffusion process is discussed and ξ is concentration. First, the diffusion process in phase A is simulated, with diffusion in phase B not allowed. For the pore-scale simulations, the Dirichlet boundary condition is adopted along the x direction, namely high and low values of concentration are applied at $x = 0$ and $x = L$, respectively, generating concentration gradient along x direction for driving the diffusion. In the LB framework, the Dirichlet boundary condition is obtained by specifying the distribution function at the inlet and outlet to its equilibrium distribution function. Periodic boundary condition is applied at the other two directions. The LB diffusion model is adopted for solving Eq. (14). The relaxation time τ is set to be unity. Effective diffusivity is predicted based on the field of ξ obtained. Fig. 5 shows the concentration distributions in phase A with different ε_A, where Phase B is the solid matrix. It can be seen that local concentration distributions are remarkably affected by the distributions of phase A. As mentioned in Section 2 and demonstrated in Section 4.1, the Gyroid structure possesses good connectivity even under very low porosity. Therefore, mass transport from inlet to the outlet still can be established even under very low value of ε_A studied in the present study ($\varepsilon_A = 0.2$), as shown in Fig. 5(c). Fig. 6 further displays the concentration fields in phase B, where phase A is the solid matrix. Again, it can be found that due to the good connectivity of phase B, there is no dead region in phase B which is not accessible to the mass transport. As ε_B increases, mass transport resistance becomes weaker in phase B. This will lead to higher values of effective diffu-

Table 1
Reynolds number of all the cases studied.

Porosity	0.1	0.2	0.3	0.4	0.5	0.6	0.7	0.8	0.9
Phase A ($\times 10^{-4}$)	1.2	5.6	14.7	29.2	49.0	76.9	115.4	161.3	222.2
Phase B ($\times 10^{-5}$)	2.8	25.5	87.2	226.5	468.0	852.2	1534.2	2478.4	5046.2

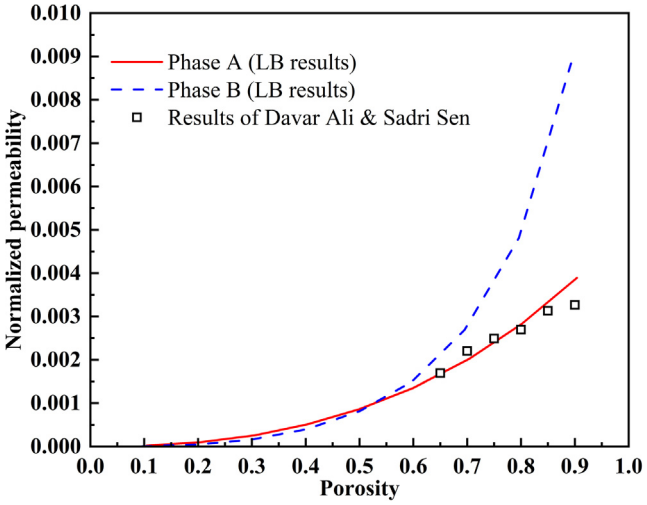

Fig. 4. Permeability of the Gyroid structure under different porosity.

sivity, as plotted in Fig. 7. The effective diffusivity Γ_{eff} is calculated based on the concentration field obtained using the following formula [39].

$$\Gamma_{eff} = \frac{(\int_0^{L_y}\int_0^{L_z}(\Gamma\frac{\partial\xi}{\partial x})|_{L_x}dydz)/L_yL_z}{(\xi_{in}-\xi_{out})/L_x} \quad (15)$$

In Fig. 7, the normalized effective diffusivity Γ_{eff}/Γ is shown in the y axis, while the porosity for phase A or B is shown in the x axis. Firstly, Γ_{eff}/Γ for cylinder porous media is predicted using the LB diffusion code, and is shown in Fig. 7. Analytical results in the literature are also displayed [47]. It can be found that the LB predicted results agree well with the analytical results, demonstrating the accuracy of our LB model and code.

For the Gyroid structure, it can be found that Γ_{eff}/Γ of phase A is lower than phase B, indicating diffusion through phase A is slower than that through phase B, consistent with the result of permeability in Fig. 4. Second, it can be found that Γ_{eff}/Γ for phase B can be well described by the Bruggeman equation widely adopted in the literature [48]

$$\Gamma_{eff} = \Gamma\frac{\varepsilon}{\tau} \quad (16)$$

where ε is the porosity. τ on the denominator is the tortuosity, which is set as ε^{α} with α as -0.5 in the original Bruggeman equation. For phase B in the Gyroid structure, α is -0.4. For phase A, however, fitting using the Bruggeman equation leads to large discrepancy, even for the best fitting curve with α as -0.9. This indicates that Bruggeman equation is not suitable for predicting effective diffusivity of phase A. The following curve for Γ_{eff}/Γ of phase A is proposed as $a(\varepsilon_A)^n$, with $a = 0.688$ and $n = 1.257$. This curve is not ideal because although it goes through (0,0), it does not go through (1,1). Therefore, it is only suitable for predicting values of effective diffusivity for ε_A in the range of 0.1 to 0.9. Finally, results of effective diffusivity for the Gyroid structure in the literature are also plotted in Fig. 7 [24]. It can be found that the results of Shen et al. [24], which were predicted using random walking method, are significantly higher than our results. The reason of such large discrepancy is not known, but we believe our results are correct as our LB diffusion model has been well validated in this study as well as in our previous studies.

4.3. Hydraulic and diffusive tortuosity

As clearly displayed in Fig. 3, the presence of solid skeleton causes the fluid flow paths to deviate from straight lines. To represent such deviation, tortuosity is proposed which provides a good understanding of fluid flow and the void space complexity in a porous medium. Higher value of tortuosity means longer and more

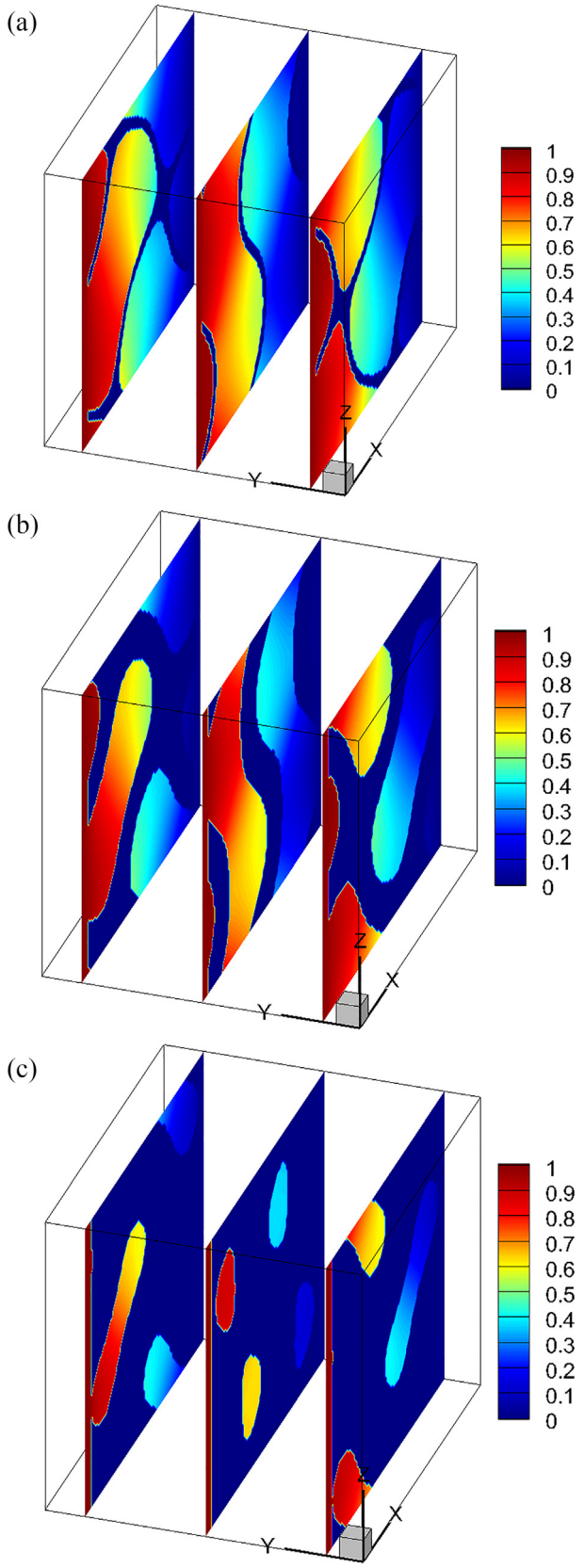

Fig. 5. Concentration filed in phase A of the Gyroid structure with different porosity. (a) $\varepsilon_A = 0.9$, (b) $\varepsilon_A = 0.6$ and (c) $\varepsilon_A = 0.2$.

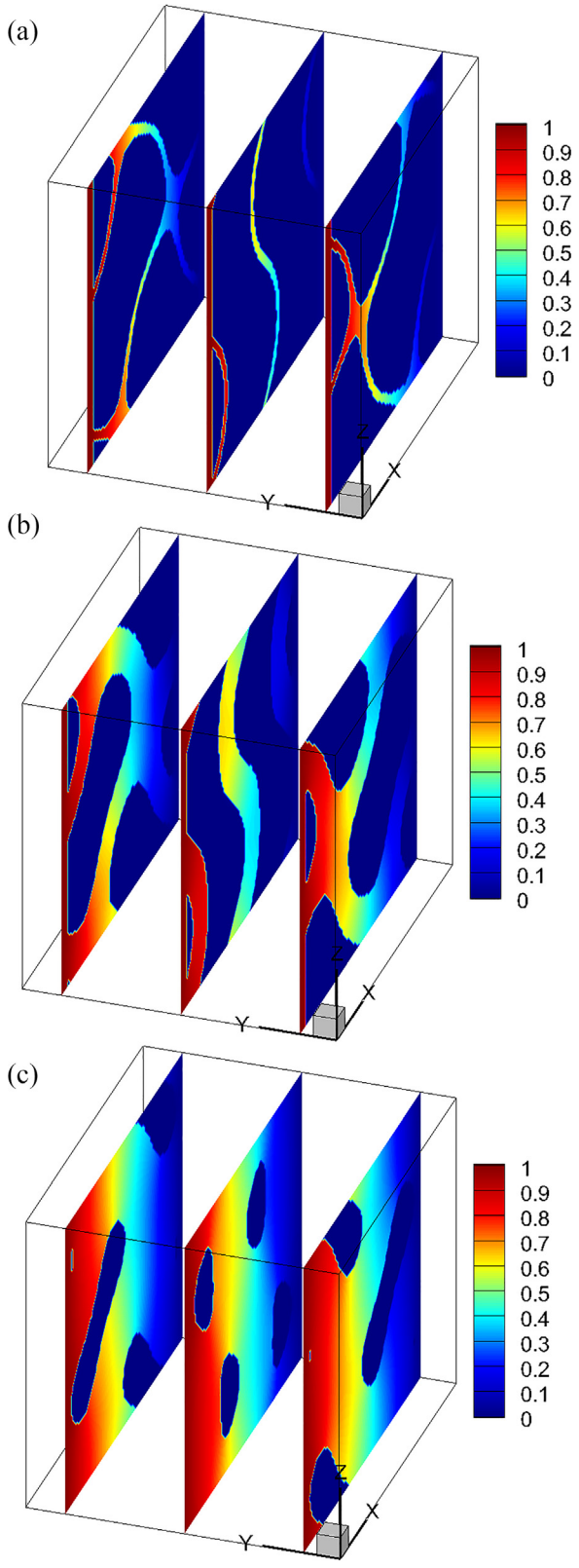

Fig. 6. Concentration filed in phase B of the Gyroid structure with different porosity. (a) $\varepsilon_B = 0.1$, (b) $\varepsilon_B = 0.4$ and (c) $\varepsilon_B = 0.8$.

tortuous pathway for fluid flowing through a porous medium. Due to the various morphology and complicated structures of porous media, there is no universal relationship between tortuosity and porosity. It is worth mentioning that tortuosity actually is a

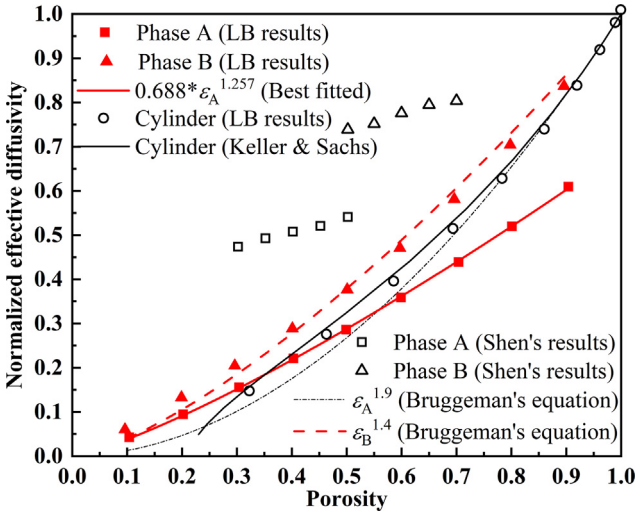

Fig. 7. Effective diffusivity of the Gyroid structure under different porosity.

process-dependent variable. This means that for the same porous medium, the value of tortuosity may be different for different transport processes studied, such as fluid flow, diffusion and electron conduction.

For fluid flow, the tortuosity is called hydraulic tortuosity. To the best of our knowledge, there has been no report on the hydraulic tortuosity of the Gyroid structure. Based on the velocity field obtained from the simulation results in Section 4.1, hydraulic tortuosity is calculated according to the following formula

$$\tau_h = \frac{\sum \sqrt{u_x^2 + u_y^2 + u_z^2}}{\sum |u_x|} \tag{17}$$

Fig. 8(a) plots the values of hydraulic tortuosity of phase A and B. The LB simulation results (dots in Fig. 8(a)) show that hydraulic tortuosity of the phase B is from about 1.19 to 1.06 when porosity changes from 0.1 to 0.9, while that of phase A varies between 1.35 and 1.20 when porosity of phase A changes from 0.1 to 0.9. The hydraulic tortuosity of phase A is relatively higher than that of phase B, consistent with the results of permeability in Fig. 4. The LB simulation results of tortuosity under different porosity are also fitted. For phase B, the following curve is obtained

$$\tau_{h,B} = 1.185 + 0.019\varepsilon_B - 0.195\varepsilon_B^2 \tag{18}$$

This curve goes through the point (1,1) and such characteristic has physical meaning. Because theoretically as the porosity approaches unity, the value of the corresponding hydraulic tortuosity will also approach unity.

The best fitted curve for phase A has the following form

$$\tau_{h,A} = 1.371 - 0.25\varepsilon_A + 0.086\varepsilon_A^2 \tag{19}$$

For this curve, the hydraulic tortuosity is about 1.207 when ε_A is unity. Such result does not agree with theoretical analysis. Nevertheless, the result is reasonable. Because for the Gyroid structure, when ε_A approaches unity (or ε_B approaches zero), the thickness of phase B approaches zero (as shown in Fig. 1); however, as long as ε_B is not zero, even if it is extremely low, phase B still exists as a continuous surface with infinitely low thickness in the domain. The complicated surface of phase B forces the fluid flow to deflect from straight line.

In Section 4.2, diffusion processes are also simulated, and the diffusive tortuosity τ_d thus is also calculated based on the pore-scale results in Fig. 7 and the Bruggeman equation Eq. (16). As shown in Fig. 8(b), the value of the diffusive tortuosity for phase

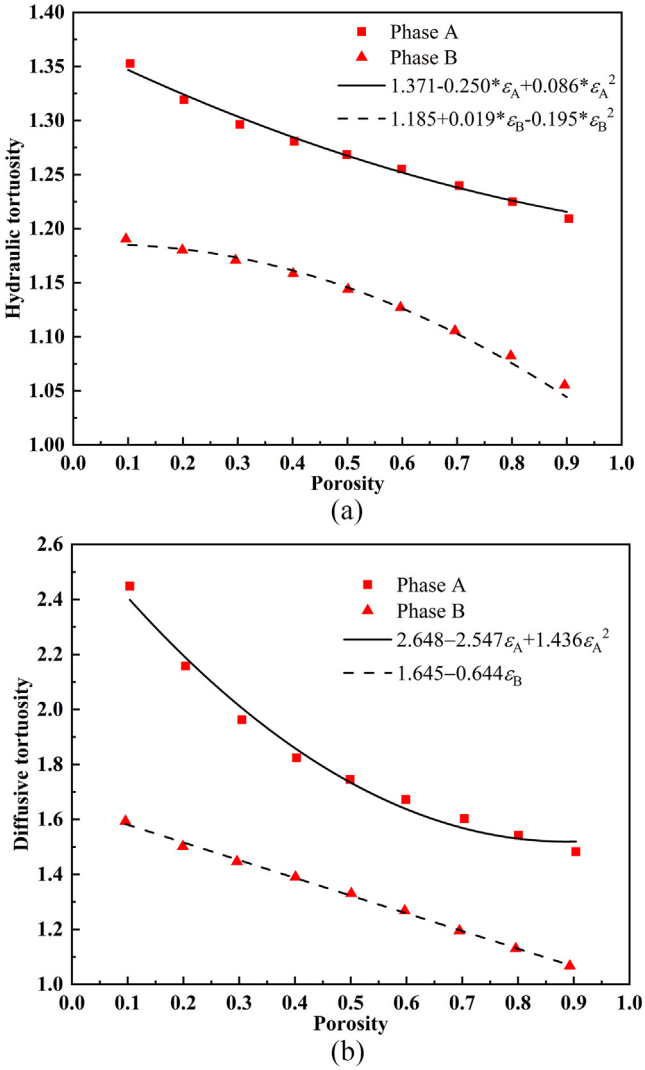

Fig. 8. Tortuosity of the Gyroid structure for (a) single-phase fluid flow and (b) diffusion processes. (a) Hydraulic tortuosity and (b) diffusive tortuosity.

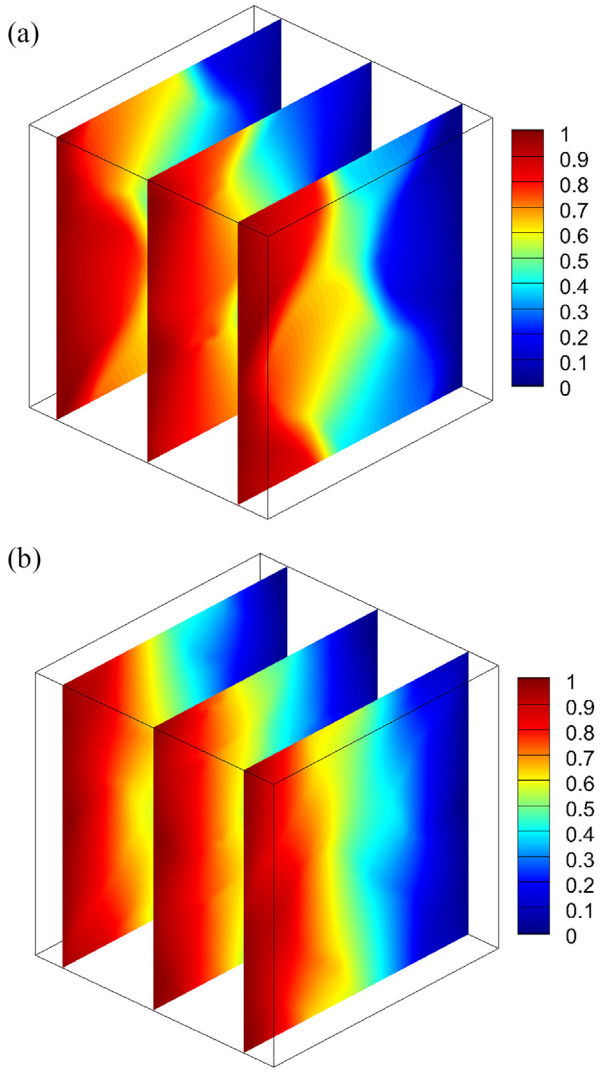

Fig. 9. Temperature field in the Gyroid structure with (a) phase A as void space and phase B as solid phase and (b) the opposite case. In Fig. 9(a), λ_A = 0.029 W m^{-1} K^{-1}, λ_B = 100 W m^{-1} K^{-1}, ε_B = 0.6, and in Fig. 9(b) the values of thermal conductivity are exchanged and the porosity keeps the same compared with Fig. 9(a).

A is between 1.48~2.44, which is much higher than that of phase B between 1.07~1.59. The best fitting curves are also plotted in Fig. 8 (b). Similar to Fig. 8(a), it can be found that for Phase B, the curve also goes through (1,1); however, this is not the case for phase A. Comparing Fig. 8(b) with Fig. 8(a), it can be found that values of diffusive tortuosity are much higher than the hydraulic tortuosity. It is worth mentioning that there are different definitions of tortuosity even for the same transport process. One should keep in mind which kind of tortuosity is studied and what is the definition of the tortuosity.

4.4. Heat conduction and effective thermal conductivity

Finally, thermal conduction process inside the Gyroid structure is studied. Note that different from fluid flow and diffusion processes which are only allowed in the void space, thermal conduction can take place in both the void space and solid phase. During the simulation, a constant temperature difference $\Delta T = 1$ between the inlet and outlet is employed, while other surfaces are supposed to be adiabatic. First, the scenario in which phase A is void phase and phase B is solid phase is studied. The thermal conductivity of phase A is fixed as 0.029 W m^{-1} K^{-1} while that of phase B is set as 1, 10, 100 and 400 W m^{-1} K^{-1}, respectively, representing different materials adopted as the solid skeleton. Fig. 9(a) shows the steady state dimensionless temperature distributions in the Gyroid structure with λ_A = 0.029 W m^{-1} K^{-1}, λ_B = 100 W m^{-1} K^{-1}, ε_B = 0.6, while that in Fig. 9(b) is with λ_A = 100 W m^{-1} K^{-1}, λ_B = 0.029 W m^{-1} K^{-1}, ε_A = 0.6. As shown in Fig. 9, temperature distributions are complicated due to the complex structures of Gyroid. Different temperatures in Fig. 9(a) and 9(b) will lead to quite different values of effective thermal conductivity, as shown in Fig. 10.

In Fig. 10, the thermal conductivity has been normalized by the corresponding thermal conductivity of the solid phase. It can be found that choosing phase B as the solid phase always leads to higher effective thermal conductivity, which agrees with the results of permeability and effective diffusivity in Section 4.1 and 4.2.

5. Conclusion

As a triply periodic minimal surface with bicontinous phases, Gyroid structures have great application potential in several fields such as fuel cells, batteries, solar cells and tissue engineering. Understanding the transport capacity of the Gyroid structure is of great importance. The two phases in Gyroid structures are both continuous, leading to bicontinuous characteristic. In the present

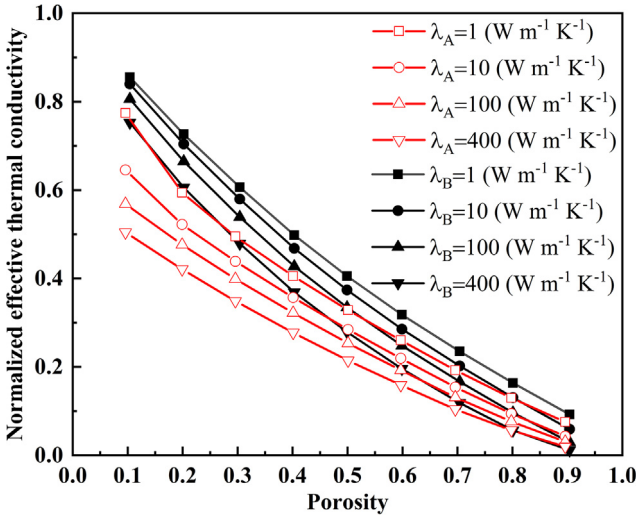

Fig. 10. Effective thermal conductivity of the Gyroid structure under different porosity.

study, fluid flow, diffusion and thermal conduction processes in each phase of the Gyroid structure are simulated. Transport properties including permeability, effective diffusivity and effective thermal conductivity are evaluated. Values of the normalized permeability for phase A (see Fig. 1 of phase A) is between $2.04 \times 10^{-5} \sim 3.89 \times 10^{-3}$, while that for phase B is between $4.89 \times 10^{-6} \sim 8.84 \times 10^{-3}$, for the range of porosity studied between 0.1~0.9. Pure diffusion process obeying the Fick's law is also simulated, and effective diffusivity is predicted. For phase B, effective diffusivity can be well described by the classical Bruggeman equation with α as -0.4, while that for phase A cannot be fitted by the Bruggeman equation. For phase A, values of the normalized effective diffusivity are between 0.042~0.61, while that for phase B is between 0.060~0.837. Effective thermal conductivity of the Gyroid structures is also predicted. It is found that choosing phase B as the solid phase facilitates heat transfer in the Gyroid structure. Values of hydraulic and diffusive tortuosity are also predicted. The results show that tortuosity in phase B is lower than that in phase A. Besides, diffusive tortuosity is higher than the hydraulic tortuosity.

Macroscopic transport properties predicted in this study is helpful for future researches planning to use Gyroid structures as transport media such as electrodes in fuel cells and batteries. Based on the results in this study, it can be found that transport resistance in phase B is lower than that in phase A. In practice, porous media with multiple components are adopted for transporting different reactants. The chemical reaction is endothermic or exothermic. For example, in cathode catalyst layer of proton exchange membrane fuel cells, solid carbon, electrolyte and pores are for transporting electron, proton and gas species, respectively. Oxygen reduction reaction takes place which releases heat, leading to higher temperature in the cathode catalyst layer [49]. Our results here suggest that it may be desirable to choose phase B as the pathway for the slowest transport process to enhance the rate-limited process.

Finally, it is worth mentioning that reactive transport processes inside the Gyroid structures with background of fuel cells and batteries are undergoing in our group. Important parameters related to reactive transport, such as the mass transfer coefficient [50], will also be evaluated in the Gyroid structure.

Declaration of Competing Interest

We declare no conflict of interest.

Acknowledgement

Li Chen thanks the support of National Natural Science Foundation of China (51776159) and National key research and development program (2017YFB0102702). Qinjun Kang acknowledges the support of LANL's LDRD Program and Institutional Computing Program.

References

[1] J. Bear, Dynamics of Fluids in Porous Media, Dover Publicaitons Inc., New York, 2013.
[2] G. Wu, K.L. More, C.M. Johnston, P. Zelenay, High-Performance electrocatalysts for oxygen reduction derived from polyaniline, iron, and cobalt, Science 332 (6028) (2011) 443–447.
[3] P. Zhang, Z.N. Meng, H. Zhu, Y.L. Wang, S.P. Peng, Melting heat transfer characteristics of a composite phase change material fabricated by paraffin and metal foam, Appl. Energy 185 (2017) 1971–1983.
[4] I. Yadroitsev, I. Shishkovsky, P. Bertrand, I. Smurov, Manufacturing of fine-structured 3D porous filter elements by selective laser melting, Appl. Surf. Sci. 255 (10) (2009) 5523–5527.
[5] F.A.L. Dullen, Porous Media: Fluid Transport and Pore Structure, Academic Press Inc, New York, 1992.
[6] W. Li, J. Liu, D. Zhao, Mesoporous materials for energy conversion and storage devices, Nat. Rev. Mater. 1 (2016) 16023.
[7] P. Jorge, M.A.A. Mendes, E. Werzner, J.M.C. Pereira, Characterization of laminar flow in periodic open-cell porous structures, Chem. Eng. Sci. 201 (2019) 397–412.
[8] L. Chen, Y. He, W.-Q. Tao, P. Zelenay, R. Mukundan, Q. Kang, Pore-scale study of multiphase reactive transport in fibrous electrodes of vanadium redox flow batteries, Electrochim. Acta 248 (2017) 425–439.
[9] C.Y. Zhao, Review on thermal transport in high porosity cellular metal foams with open cells, Int. J. Heat Mass Transf. 55 (13) (2012) 3618–3632.
[10] K.J. Maloney, K.D. Fink, T.A. Schaedler, J.A. Kolodziejska, A.J. Jacobsen, C.S. Roper, Multifunctional heat exchangers derived from three-dimensional micro-lattice structures, Int. J. Heat Mass Transf. 55 (9) (2012) 2486–2493.
[11] A. Schoen, Infinite periodic minimal surfaces without self-intersections, NASA Technical Note TN D-5541, (1970).
[12] W. Longley, T.J. McIntosh, A bicontinuous tetrahedral structure in a liquid-crystalline lipid, Nature 303 (5918) (1983) 612–614.
[13] V. Saranathan, C.O. Osuji, S.G.J. Mochrie, H. Noh, S. Narayanan, A. Sandy, E.R. Dufresne, R.O. Prum, Structure, function, and self-assembly of single network gyroid photonic crystals in butterfly wing scales, Proc. Natl. Acad. Sci. 107 (26) (2010) 11676–11681.
[14] J. Kibsgaard, Ariel Jackson, Thomas F. Jaramillo, Mesoporous platinum nickel thin films with double gyroid morphology for the oxygen reduction reaction, Nano Energy 29 (2016) 243–248.
[15] E.J.W. Crossland, M. Kamperman, M. Nedelcu, C. Ducati, U. Wiesner, D.M. Smilgies, G.E.S. Toombes, M.A. Hillmyer, S. Ludwigs, U. Steiner, H.J. Snaith, A bicontinuous double gyroid hybrid solar cell, Nano Lett. 9 (8) (2009) 2807–2812.
[16] T. Ichikawa, T. Kato, H. Ohno, 3D continuous water nanosheet as a Gyroid minimal surface formed by bicontinuous cubic liquid-crystalline zwitterions, J. Am. Chem. Soc. 134 (28) (2012) 11354–11357.
[17] S. Choudhury, M. Agrawal, P. Formanek, D. Jehnichen, D. Fischer, B. Krause, V. Albrecht, M. Stamm, L. Ionov, Nanoporous cathodes for high-energy Li–S batteries from Gyroid block copolymer templates, ACS Nano 9 (6) (2015) 6147–6157.
[18] Q. Gao, X.-L. Wang, J. Xu, X.-H. Bu, The first demonstration of the Gyroid in a polyoxometalate-based open framework with high proton conductivity, Chem. – A Eur. J. 22 (27) (2016) 9082–9086.
[19] J.G. Werner, G.G. Rodríguez-Calero, H.D. Abruña, U. Wiesner, Block copolymer derived 3-D interpenetrating multifunctional gyroidal nanohybrids for electrical energy storage, Energy Environ. Sci. 11 (2018) 1261–1270.
[20] D. Ali, S. Sen, Finite element analysis of mechanical behavior, permeability and fluid induced wall shear stress of high porosity scaffolds with gyroid and lattice-based architectures, J. Mech. Behav. Biomed. Mater. 75 (2017) 262–270.
[21] A. Xu, W. Shyy, T. Zhao, Lattice Boltzmann modeling of transport phenomena in fuel cells and flow batteries, Acta Mech. Sin. 33 (3) (2017) 555–574.
[22] A.L. Olivares, È. Marsal, J.A. Planell, D. Lacroix, Finite element study of scaffold architecture design and culture conditions for tissue engineering, Biomaterials 30 (30) (2009) 6142–6149.
[23] S. Ma, Q. Tang, Q. Feng, J. Song, X. Han, F. Guo, Mechanical behaviours and mass transport properties of bone-mimicking scaffolds consisted of gyroid structures manufactured using selective laser melting, J. Mech. Behav. Biomed. Mater. 93 (2019) 158–169.
[24] K.-H. Shen, J.R. Brown, L.M. Hall, Diffusion in lamellae, cylinders, and double Gyroid block copolymer nanostructures, ACS Macro Lett. 7 (9) (2018) 1092–1098.
[25] D. Zhang, R. Zhang, S. Chen, W.E. Soi, Pore scale study of flow in porous media: Scale dependency, REV, and statistical REV, Geophys. Res. Lett. 27 (2) (2000) 1195–1198.

[26] K. Vafai, S. Kim, On the limitations of the Brinkman-Forchheimer-extended Darcy equation, Int. J. Heat Fluid Flow 16 (1) (1995) 11–15.
[27] M.J. Blunt, B. Bijeljic, H. Dong, O. Gharbi, S. Iglauer, P. Mostaghimi, A. Paluszny, C. Pentland, Pore-scale imaging and modelling, Adv. Water Resour. 51 (2013) 197–216.
[28] H. Li, C. Pan, C.T. Miller, Pore-scale investigation of viscous coupling effects for two-phase flow in porous media, Phys. Rev. E 72 (2) (2005) 026705.
[29] Q. Kang, P.C. Lichtner, D. Zhang, Lattice Boltzmann pore-scale model for multicomponent reactive transport in porous media, J. Geophys. Res. Solid Earth 111 (B5) (2006).
[30] A.M. Tartakovsky, P. Meakin, Pore scale modeling of immiscible and miscible fluid flows using smoothed particle hydrodynamics, Adv. Water Resour. 29 (10) (2006) 1464–1478.
[31] S.Y. Chen, G.D. Doolen, Lattice Boltzmann methode for fluid flows, Ann. Rev. Fluid Mech. 30 (1998) 329–364.
[32] L. Chen, Q. Kang, Y. Mu, Y.-L. He, W.-Q. Tao, A critical review of the pseudopotential multiphase lattice Boltzmann model: methods and applications, Int. J. Heat Mass Transf. 76 (2014) 210–236.
[33] J. Zhang, Lattice Boltzmann method for microfluidics: models and applications, Microfluid. Nanofluid. 10 (1) (2011) 1–28.
[34] Wikipedia, Gyroid, in, https://en.wikipedia.org/wiki/Gyroid.
[35] H.-Y. Chen, Y. Kwon, K. Thornton, Multifunctionality of three-dimensional self-assembled composite structure, Scr. Mater. 61 (2009) 52–55.
[36] D. d'Humières, Multiple–relaxation–time lattice Boltzmann models in three dimensions, Philosoph. Trans. R. Soc. Lond. A: Math. Phys. Eng. Sci. 360 (1792) (2002) 437–451.
[37] D. d'Humières, I. Ginzburg, M. Krafczyk, P. Lallemand, L.-S. Luo, Multiple–relaxation–time lattice Boltzmann models in three dimensions, Philosoph. Trans. R. Soc. Lond. Ser. A: Math. Phys. Eng. Sci. 360 (1792) (2002) 437–451.
[38] L. Chen, G. Wu, E.F. Holby, P. Zelenay, W.-Q. Tao, Q. Kang, Lattice Boltzmann pore-scale investigation of coupled physical-electrochemical processes in C/Pt and non-precious metal cathode catalyst layers in proton exchange membrane fuel cells, Electrochim. Acta 158 (2015) 175–186.
[39] L. Chen, L. Zhang, Q. Kang, H.S. Viswanathan, J. Yao, W. Tao, Nanoscale simulation of shale transport properties using the lattice Boltzmann method: permeability and diffusivity, Sci. Rep. 5 (2015) 8089.
[40] L. Chen, R. Zhang, P. He, Q. Kang, Y.-L. He, W.-Q. Tao, Nanoscale simulation of local gas transport in catalyst layers of proton exchange membrane fuel cells, J. Power Sources 400 (2018) 114–125.
[41] W.-Z. Fang, L. Chen, J.-J. Gou, W.-Q. Tao, Predictions of effective thermal conductivities for three-dimensional four-directional braided composites using the lattice Boltzmann method, Int. J. Heat Mass Transf. 92 (2016) 120–130.
[42] Z. Guo, B. Shi, C. Zheng, A coupled lattice BGK model for the Boussinesq equations, Int. J. Numer. Meth. Fluids 39 (4) (2002) 325–342.
[43] S. Whitaker, Flow in porous media I: a theoretical derivation of Darcy's law, Transp. Porous Media 1 (1) (1986) 3–25.
[44] L. Chen, W. Fang, Q. Kang, J. De'Haven Hyman, H.S. Viswanathan, W.-Q. Tao, Generalized lattice Boltzmann model for flow through tight porous media with Klinkenberg's effect, Phys. Rev. E 91 (3) (2015), 033004.
[45] L.J. Klinkenberg, The permeability of porous media to liquids and gases, Drilling and Production Practice, American Petroleum Institute, New York, New York, USA, 1941.
[46] P. Paradisi, R. Cesari, F. Mainardi, F. Tampieri, The fractional Fick's law for non-local transport processes, Phys. A 293 (1–2) (2001) 130–142.
[47] H.B. Keller, D. Sachs, Calculations of the conductivity of a medium containing cylindrical inclusions, J. Appl. Phys. 35 (3) (1964) 537–538.
[48] D.-W. Chung, M. Ebner, D.R. Ely, V. Wood, R.E. García, Validity of the Bruggeman relation for porous electrodes, Modell. Simul. Mater. Sci. Eng. 21 (7) (2013) 074009.
[49] L. Chen, Q. Kang, W. Tao, Pore-scale study of reactive transport processes in catalyst layer agglomerates of proton exchange membrane fuel cells, Electrochim. Acta 306 (2019) 454–465.
[50] A. Xu, T. Zhao, L. Shi, J. Xu, Lattice Boltzmann simulation of mass transfer coefficients for chemically reactive flows in porous media, J. Heat Transf. 140 (5) (2018) 052601.